


Duplex n- and p-Type Chromia Grown on Pure Chromium: A Photoelectrochemical and Microscopic Study

L. Latu-Romain¹  · Y. Parsa¹ · S. Mathieu² ·
M. Vilasi² · M. Ollivier¹ · A. Galerie¹ · Y. Wouters¹

Received: 18 July 2016/Revised: 26 August 2016/Published online: 2 September 2016
© Springer Science+Business Media New York 2016

Abstract Chromia grown on pure chromium at 900 °C for 30 min at an oxygen partial pressure $p(\text{O}_2)$ of 10^{-12} atm has been characterized using photoelectrochemical and electron microscopy techniques. This study reveals a duplex scale: n-chromia with equiaxis morphology in the internal part (~ 650 nm thick) and p-chromia with columnar morphology in the external part (~ 900 nm thick). Grain orientation maps also revealed the presence of a c-oriented chromia layer at the interface between the n- and the p-subscales. This $\langle 0001 \rangle$ textured layer was identified as the first-grown chromia layer. It means that internal n-equiaxis chromia grew by anionic transport governed by oxygen vacancy diffusion, whereas external p-columnar chromia layer grew outwards and was controlled by chromium vacancy diffusion.

Keywords Chromia · Photoelectrochemistry · TEM characterizations · Point defects

Introduction

Metallic materials, such as stainless steels, are submitted to high temperature and harsh environments and their chemical durability generally depends on the nature of the point defects that ensure the matter transport through the oxide layers developed on their surfaces. The growth of a thermal oxide is indeed generally limited by point defects diffusion [1] and the oxidation resistance of these metallic materials relies generally on the formation of dense and adherent chromia (-or alumina-) scales [2].

✉ L. Latu-Romain
laurence.latu-romain@simap.grenoble-inp.fr

¹ University Grenoble Alpes, CNRS, SIMAP, 38000 Grenoble, France

² IJL, University of Lorraine, 54011 Nancy, France

Nevertheless, chromium exhibits a complex oxidation behavior. Chromia has, in fact, a complicated defect structure and its electronic and structural properties have been the subject of many investigations for long time [3, 4]. From electrical conductivity on sintered chromia, it has been assessed that chromia is an intrinsic electronic conductor at temperature superior or equal to 1000 °C in a large range of oxygen activity [5, 6]. It is also well known, from Kofstad studies [3] and later measured by photoelectrochemistry [7], that chromia has a dual character and can be n or p depending on oxidation conditions. Results on mass transport through chromia extracted from chromium oxidation studies were reviewed by Lillerud and Kofstad in their first 1980 paper [8]. These authors suggested, as previously proposed by Caplan and Sproule [9], that both chromium and oxygen are mobile in chromia. However, the major point defects responsible for its growth remain still unknown and difficult to determine. Indeed, to identify and to be able to measure the nature of the point defects remains very difficult. For that purpose, photoelectrochemistry is an interesting experimental technique because it permits to measure the semiconducting properties of the oxide [10] which depend on the point defect that constitute the passive layer [11, 12]. Taking advantage of the present knowledge on chromia [7, 13] and using photoelectrochemical and TEM characterization techniques, we propose in this work to have a careful look at a n- and p-type chromia, further denominated as a “duplex chromia” in order to discuss possible mechanism for its growth.

Experimental Procedures

To grow a chromia layer, pure chromium (99.99 % purity, from Goodfellow S.A.R.L., France) has been oxidized. Before oxidation tests, Cr samples were cut from a plate to the dimension $10 \times 10 \times 1 \text{ mm}^3$ and were SiC ground up to the grade 320. Samples were then oxidized at 900 °C at a rather low and controlled oxygen partial pressure. For that purpose, the samples were placed on an alumina crucible itself positioned in a silica tube containing NiO bunsenite/nickel buffering powder mixture to control the oxygen activity during the oxidation step. Before being sealed, the silica tube had been locally reduced in section to prepare the sealing, and then connected to a vacuum station. Once the pressure value falls below $\sim 10^{-8}$ atm, the tube was Ar-filled so that the pressure reaches around 0.25 atm (to have a total pressure in the tube of ~ 1 atm at the oxidation temperature of 900 °C), then sealed. Finally, sealed tubes were placed in a muffle furnace at 900 °C for 30 min then cooled in air. Thermodynamic calculations based on the total Gibbs free energy minimization were carried out with the Factsage 7.0TM software using a coherent set of pure substances from the FACT pure substances database [11]. At 900 °C, the calculated equilibrium oxygen partial pressure $p(\text{O}_2)$ imposed by the buffer is equal to 10^{-12} atm. The choice of the $p(\text{O}_2)$ and temperature has here been selected in order to possibly grow a duplex n- and p-type chromia layer [13]. In these conditions, oxide scale thickness can be estimated in the micrometer range.

After cooling the samples, the semiconducting properties of the oxide layer were measured by photoelectrochemistry (PEC). For macroscopic measurements, the

photocurrent was recorded as a function of photon energy, the wavelengths investigated varied by 1 nm step in the range of 220–640 nm (~ 2 –5.5 eV). All potential values indicated in this paper are always given with respect to the reference electrode (a mercury–mercurous sulfate electrode MSE, +0.650 V vs. Standard Hydrogen Electrode SHE). Microscopic PEC measurements have been carried out using a monochromatic light from an argon laser delivering two main lines in the UV: $E = 3.41$ and 3.53 eV. The beam was focused onto the surface of the oxidized chromium via the objective of an inverted microscope (spot size $\sim 1 \mu\text{m}$). The image was built by moving the sample placed on a high-resolution XY motorized stage. The same electrochemical cell as in the macroscopic PEC setup was used; these experimental setups have been already and largely detailed in references [11, 14]. The depth penetration of the light in chromia being larger than $1 \mu\text{m}$, it is reasonable to assume that the whole scale is probed during PEC experiments.

The precession-assisted crystal orientation mapping technique, ASTAR, a TEM-based diffraction spot recognition technique [15] has been used to acquire orientation maps of the oxide scale with a probe size of 1 nm and a step size of 3 nm. For that purpose, a transversal cross-section thin lamella was prepared using a dual-focused ion beam scanning electron microscope (FIB-SEM, Zeiss Cross Beam NVision 40). Details of the FIB-SEM preparation are given in the Ref. [12]. ASTAR observations coupled to STEM investigations have been conducted on a Transmission Electron Microscope at 200 keV (FEG-TEM, Jeol 2100F).

Results

Microscopic and Photoelectrochemical Characterization

The surface morphology of the scale oxidized at 900 °C during 30 min at a $p(\text{O}_2)$ of 10^{-12} atm is shown in Fig. 1a with its corresponding Raman spectrum (Fig. 1b), in

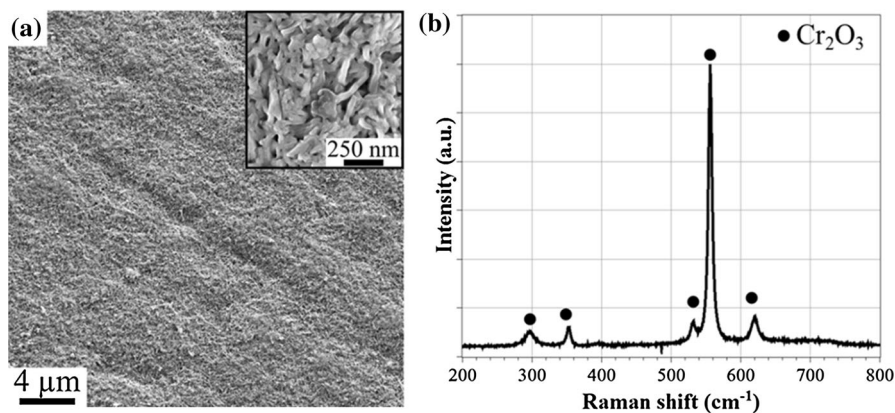


Fig. 1 Cr sample oxidized at 900 °C for 30 min at a $p(\text{O}_2)$ of 10^{-12} atm. **a** Top view SEM image of the Cr_2O_3 scale (SE detector). Inset: high-resolution SEM image of the vernacular morphology. **b** Raman (Ar + laser) spectrum of the oxidized Cr, with the characteristic bands of Cr_2O_3

well accordance with the expected vibrational bands of chromia [16]. The surface of the chromia is slightly rough with a vernacular morphology composed of faceted elongated grains (see Fig. 1a).

Figure 2 presents the cross-sectional STEM images of the oxide scale. The layer has a thickness of about 1.5 μm . On the bright-field STEM image (Fig. 2a) two distinct morphologies can be distinguished: equiaxis in the internal part (with a thickness of about 650 nm) and columnar (with a thickness of about 900 nm) in the external part, both separated by an interface. At higher magnification (dark-field, Fig. 2b), some voids could be suspected along this interface. Other large voids (~ 100 nm) are found either in the equiaxis part or in the columnar layer.

To go further, ASTAR was used in order to assess grain orientations. On the orientation maps obtained by this technique (Fig. 3a, b), the duplex structure is confirmed. Additionally, the maps reveal the presence of a textured chromia layer (red) which constitutes an interphase between equiaxis and columnar subscales. This interphase (with a thickness of about 150 nm and grain size of about 60 nm) is oriented along the c -axis of the chromia: the c -axis of the chromia is perpendicular to the metal/oxide interface. Equiaxis chromia grains have a typical size of about 250 nm, whereas columnar chromia grains have a width of about 80 nm and a length of about 750 nm. Equiaxis chromia grains are highly polycrystalline and present many different crystallographic orientations, whereas columnar chromia grains have a slight tendency to be $\langle 1100 \rangle$ oriented. Chromium grains have a typical size of about a few microns and are mainly $\langle 111 \rangle$ oriented.

It should be underlined that the oriented chromia layer in the interphase has not been observed only once: on all the recorded orientation maps (not presented in this work) a textured chromia layer was systematically detected between the equiaxis and the columnar layers.

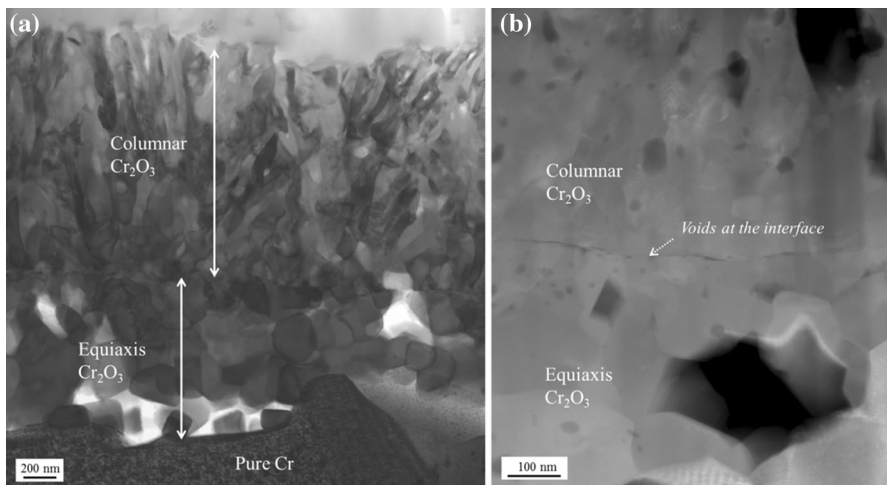


Fig. 2 **a** Bright-field cross sectional STEM image at 200 keV of Cr_2O_3 grown on pure Cr at a $p(\text{O}_2)$ of 10^{-12} atm at 900 $^\circ\text{C}$ during 30 min. **b** Dark-field cross-sectional STEM image at 200 keV: observation of voids (in black) at the intermediate interface between the equiaxis and columnar chromia layers

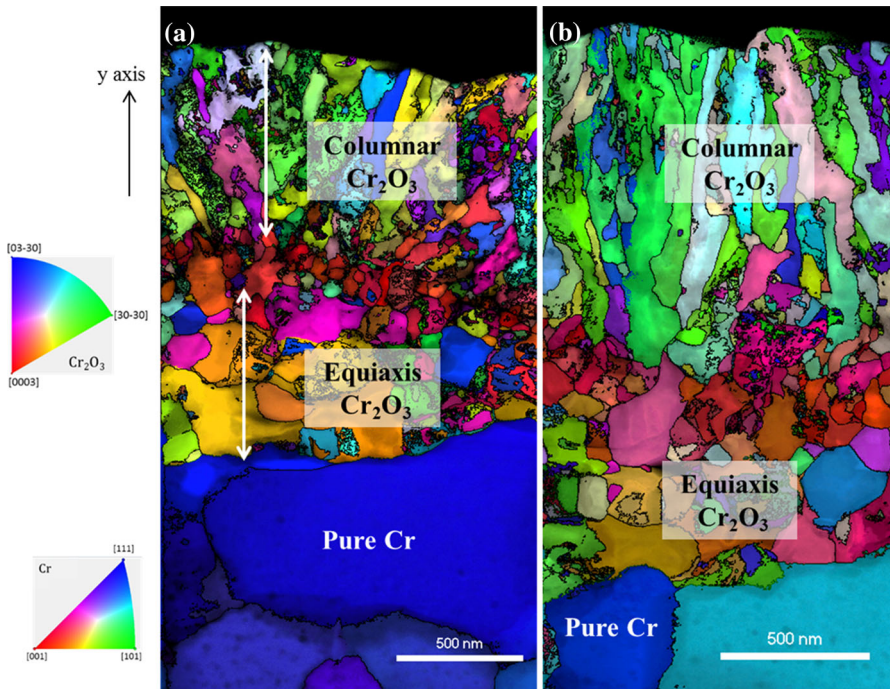


Fig. 3 ASTAR grain orientation maps (see color codes on the left) of Cr₂O₃ grown on pure Cr at a $p(\text{O}_2)$ of 10^{-12} atm at 900 °C during 30 min recorded with a probe size of 1 nm and a step size of 3 nm, **a** and **b** representing two different areas recorded along the thin lamella

Figure 4a presents photoelectrochemical responses of the chromia layer as a function of light energy E recorded at several applied potentials V . It is shown that the oxide scale is composed of two kinds of chromia with different semiconducting properties: a n- and a p-type chromia which bandgaps are classically reported, respectively, near 3.0 (contribution C_1) and 3.5 eV (contribution C_2) [7]. The change of semiconduction from n- to p- type when incident energy increases can be observed on these spectra by the change of the dephasing angle of the photocurrent of 180° (observed at about 3.3 eV in Fig. 4b). Evolution of the photocurrent as a function of the applied potential (Fig. 4c, d) confirms the type of semiconduction. At C_1 and C_2 maxima; 3.15 eV (resp. 4.75 eV) the photocurrent increases with anodic (resp. cathodic) potential and confirms the n-type (resp. p-type) semiconduction.

Flat-band potentials of contributions C_1 and C_2 have also been determined from Fig. 4c, d. The works of Gärtner [17] and Butler [18] showed that the photocurrent can be expressed as

$$I_{ph} = e \cdot J_0 \cdot \alpha_\lambda \cdot W_{SC} = e \cdot J_0 \cdot \alpha_\lambda \cdot \sqrt{\frac{2\epsilon\epsilon_0}{N \cdot e}} \sqrt{V - V_{fb}}, \quad (1)$$

where e is the elementary charge of the electron, J_0 the incident photon flux, α_λ the absorption coefficient of the light at the wavelength λ , W_{SC} the width of the space

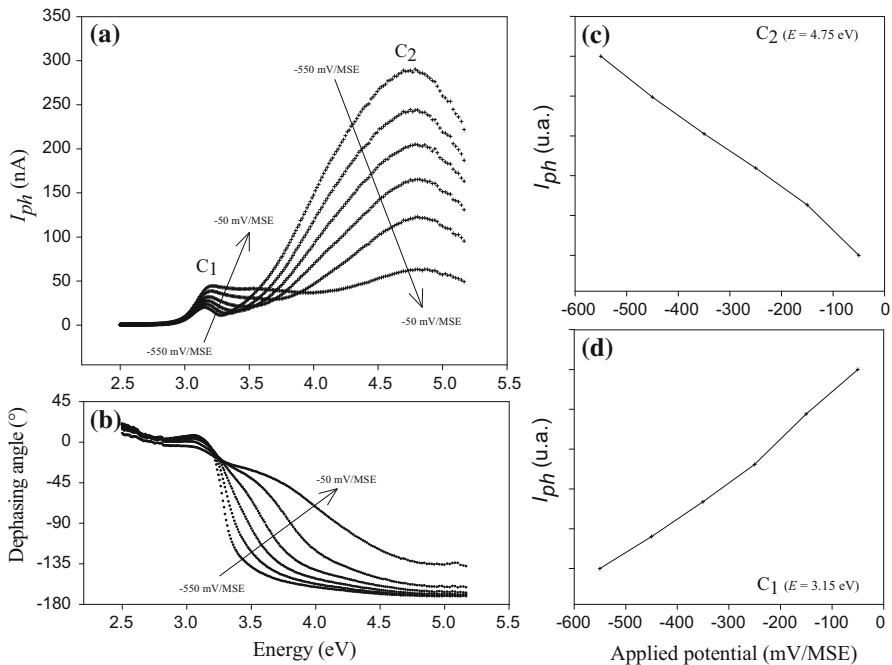


Fig. 4 **a** Photocurrent (I_{ph}) and **b** dephasing angle versus incident light energy (E) recorded at several applied potentials (V) varying from -550 mV/MSE to -50 mV/MSE with a 100 mV step-, **c** and **d** photocurrent versus applied potential (V) at 3.15 and 4.75 eV. Responses were obtained from pure Cr oxidized at 900 °C during 30 min at a $p(O_2)$ of 10^{-12} atm

charge layer, N the majority carrier density, V the applied potential, and V_{fb} the flat-band potential.

If the squared photocurrent I_{ph}^2 is plotted as a function of the applied potential V , all terms are supposed to be constants and the linear extrapolation $I_{ph}^2 = 0$ supplies the value of V_{fb} . However, the linearity of $I_{ph}^2 = f(V)$ is rarely observed experimentally, and the applied potential value of the photocurrent onset is usually taken as the value of V_{fb} . In the present case, from Fig. 4c, d, the flat-band potential of C₁ (resp. C₂) is estimated at -600 mV/MSE (resp. 0 mV/MSE) for n-chromia (resp. p-chromia). The semiconducting properties (bandgaps and flat-band potentials) of contributions C₁ and C₂ are reported in Table 1.

Various options are open about the distribution of n- and p-chromia in the oxide scale. In order to discuss this issue, microscopic PEC measurements have been carried out. Figure 3 presents two photocurrent images recorded on chromia at the same location. Concerning Fig. 5a, incident energy ($E = 3.41$ eV, lower than the bandgap of C₂) and applied potential ($V = -50$ mV/MSE) have been chosen in order to magnify C₁. This image reveals a substantially homogeneous distribution of n-chromia in the scale. Little variations recorded may be attributed to the thickness heterogeneity and surface roughness which might influence photocurrent and adsorption coefficient of the light. Regarding Fig. 5b, the situation is more complex. The argon laser used in this work does not permit to generate energy higher than

Table 1 Semiconducting properties of oxide phases detected on pure Cr oxidized at 900 °C during 30 min at a $p(\text{O}_2)$ of 10^{-12} atm

| Contribution | Maximum energy of the contribution (eV) | Oxide phase | V_{fb} (mV/MSE) | E_g (eV) |
|----------------|---|-------------|-------------------|------------|
| C ₁ | 3.15 | n-chromia | ~−600 | ~3.0 |
| C ₂ | 4.75 | p-chromia | ~0 | ~3.5 |

3.53 eV. This value, just a little higher than the bandgap of C₂ and V (−550 mV/MSE) have been chosen in order to magnify C₂ but C₁ remains probably dominant in this second image. Again, a homogeneous distribution can be observed. However, Fig. 5c, d present photocurrent versus applied potential responses extracted from zone 1 and 2 of Fig. 5b. These two zones correspond to the I_{ph} extrema (max. for zone 1 and min. for zone 2). Response of zone 1 increases monotonically and indicates the presence of n-type chromia (C₁), while v-shaped response of zone 2 reveals the presence of both n- and p-type chromia (C₁ + C₂). This result is interesting but it remains difficult to conclude on the possible distribution of

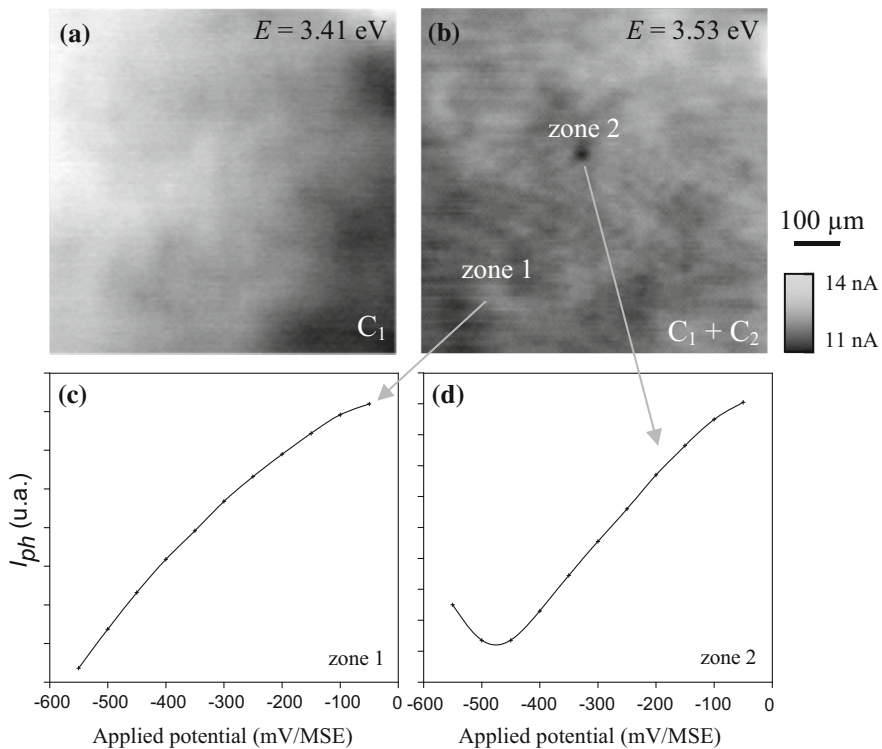


Fig. 5 Photocurrent images $510 \times 510 \mu\text{m}^2$ (point spacing: $5 \mu\text{m}$), performed on pure Cr oxidized at 900 °C during 30 min at a $p(\text{O}_2)$ of 10^{-12} atm. **a** $E = 3.41$ eV, $V = -50$ mV/MSE, **b** $E = 3.53$ eV, $V = -550$ mV/MSE. **c** and **d** photocurrent versus applied potential responses extracted from zone 1 and 2 of Fig. 3b

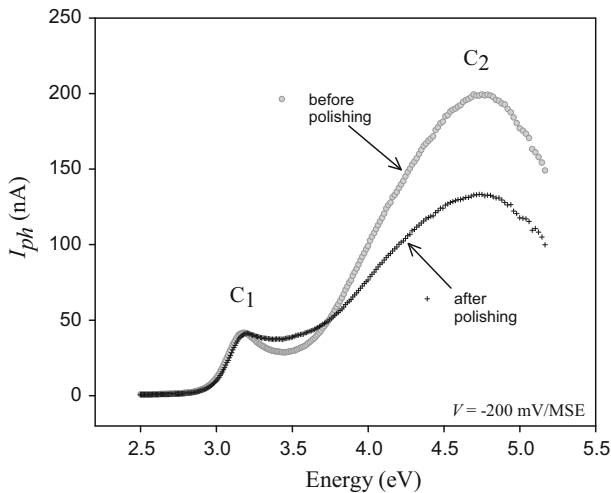


Fig. 6 Photocurrent (I_{ph}) versus incident light energy (E) recorded at -200 mV/MSE of chromia scale grown on pure Cr at 900 °C during 30 min at a $p(\text{O}_2)$ of 10^{-12} atm before and after a polishing treatment with diamond paste ($1/4$ μm) during 60 s

chromia semiconducting phases especially considering the energy of image 3b very close to the bandgap of p-type chromia.

In order to continue the discussion about the distribution of n- and p-chromia in the oxide scale, polishing of the chromia layer with diamond paste ($1/4$ μm) for 60 s has been performed. The cross-sectional SEM observation (result not presented here) reveals that only a small part of the scale has been removed after this treatment (in the range of 10 %). Figure 6 presents photocurrent versus energy responses ($V = -200$ mV/MSE) before and after this treatment. After polishing, photocurrent at the maximum energy of C_2 (4.75 eV) has decreased, whereas the one at the maximum energy of C_1 (3.15 eV) remains identical. This experimental result tends to show that p-chromia is located in the external part of the oxide scale.

Discussion

Microscopic studies have revealed in this work a peculiar structure with:

- a pure chromium substrate, textured with a $\langle 111 \rangle$ orientation, probably the result of the process used during elaboration (manufacturing method not supplied by the chromium producer),
- an internal equiaxis oxide scale with large grains (# 250 nm),
- a c-oriented interphase with small grains (# 60 nm),
- an external columnar oxide scale with long grains (# 750 nm).

On the other hand, photoelectrochemical studies have shown that chromia exhibits a dual semiconduction with a n-type (bandgap # 3.0 eV) and a p-type

contribution (bandgap \approx 3.5 eV). Micro-photoelectrochemical images have suggested a homogeneous lateral distribution of these contributions while a polishing sequence has evidenced a depth distribution: n-chromia (resp. p-chromia) located in the internal (resp. external) part. This proposal appears in good agreement with the literature. Indeed, as far as chromia growth is limited by solid-state diffusion, a fact undoubtedly recognized in the literature [19, 20], oxygen activity decreases along the scale until it reaches about 10^{-24} atm at 900 °C at the chromium/chromia interface. It is also known that for a very low oxygen activity a single n-chromia is grown, whereas for higher $p(\text{O}_2)$ n- and p-chromia are grown [13]. All these considerations tend to confirm that n-chromia is distributed in the internal part, whereas p-chromia is distributed in the external part of the scale.

At this step, it is in consequence attractive to attribute the equiaxis chromia layer to be n-type and the columnar chromia part to be p-type. Under these circumstances, the textured interphase may represent the first chromia layer grown on pure Cr. The reason for its favored orientation toward y direction (see Fig. 3) may be explained by surface energy minimization (c-oriented chromia planes are indeed polar), probably in link with the Cr substrate orientation.

Proposed Mechanism for the Growth of Duplex Chromia

It may now be considered that the scale has a duplex structure composed of an internal (resp. external) n-chromia (resp. p-chromia) with an equiaxis (resp. columnar) morphology, both separated by a textured interphase. This textured chromia layer, located in the middle of the chromia layer, is certainly the oldest chromia layer and can finally be used as a natural marker of oxide growth. In that context, equiaxis morphology can be the result of a strained inward growth (the internal subscale grows toward the metal), whereas columnar morphology reflects much more a relaxed outward growth (the external subscale grows toward the free surface). The type of semiconduction associated to the chromia growth direction makes now possible to assign the major point defect responsible for each chromia growth (see Table 2). The major point defect coming from the n-chromia is identified as oxygen vacancy, whereas the major point defect for the p-chromia growth is chromium vacancy.

The literature is controversial regarding the major point defect, especially in n-chromia. Chromium has been first supposed to diffuse by an interstitial mechanism [22]. Works using atomic simulations have concluded that anion Frenkel and Schottky disorders are less energy consuming than cation Frenkel disorder [23]. More recently, it has been demonstrated [4] that Cr Frenkel defects are more stable than Cr and O vacancies. However, a recent work [24] has demonstrated that oxygen vacancy was the predominant defect because of an anionic growth of a n-chromia grown on a Fe–Ni–Cr alloy at low $p(\text{O}_2)$ at 1000 °C. In the present work, experimental results are consistent with the presence of oxygen and chromium vacancies in a duplex chromia, a case that has been also supposed in another study conducted on NiCr model alloy [13]. In order to elucidate how the predominant defects can change from oxygen vacancy to chromium vacancy with the increase of oxygen partial pressure in the Cr_2O_3 scale, the Brouwer diagram

Table 2 Major point defects in chromium oxide depending on its type of semiconduction and oxide growth direction, adapted from [21]

| Oxide growth direction | Major point defect | Semiconducting type | Nature |
|------------------------|--------------------|---------------------|--------------------------------|
| Inward | Anionic | p | O_i'' |
| | | n | $V_O^{\bullet\bullet}$ |
| Outward | Cationic | n | $Cr_i^{\bullet\bullet\bullet}$ |
| | | p | V_{Cr}^{\bullet} |

regarding such situation is presented hereafter (Fig. 7). In Table 3, the different reactions that can occur at the external oxide/gas interface are summed up with their corresponding mass-action term. Three of the four equations of Table 3 are independent; the Schottky equilibrium is a linear combination of the first three ones. The fourth equation is provided by the electroneutrality condition: $3 [V_{Cr}^{\bullet\bullet\bullet}] + [e'] = 2 [V_O^{\bullet\bullet}] + [h^*]$. The Brouwer approximation method is used to express the point defects concentration as a function of oxygen activity, and make possible to establish the Brouwer diagram presented in Fig. 7 (the results of calculation is fully presented in Ref. [13]). At low (resp. high) $p(O_2)$, the major point defect is the oxygen (resp. chromium) vacancy and Cr_2O_3 exhibits a n-type (resp. p-type) semiconduction. Both oxygen and chromium vacancy concentrations are low and

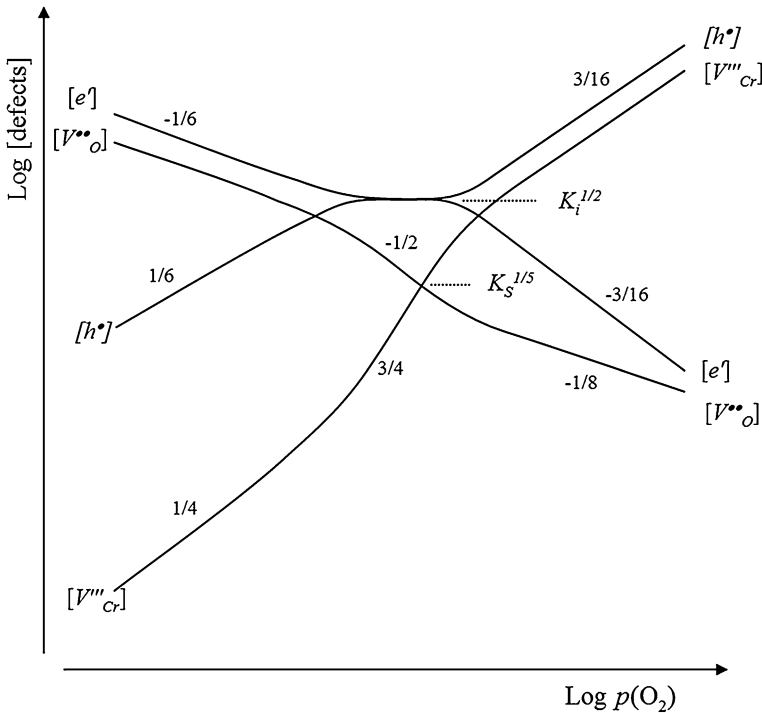


Fig. 7 Brouwer diagram of Cr_2O_3 based on a Schottky disorder. The electronic defects are predominant at the stoichiometric composition: $K_i \gg K_S$

close around the stoichiometry. In this diagram, electronic oxide defects are considered to be predominant at the stoichiometric composition ($K_i \gg K_S$), in accordance with previous studies from Holt & Kofstad [6].

As a consequence, a complete mechanism for the growth of duplex n- and p-chromia scale is proposed according to the Eqs. from 1 to 5 presented in Table 4. At the external interface, after a dissociative sorption of molecular oxygen (Eq. 1), $V_O^{\bullet\bullet}$ are consumed (Eq. 2) and $V_{Cr}^{\bullet\bullet}$ are created (Eq. 3). At the internal interface, $V_O^{\bullet\bullet}$ are created (Eq. 4) and $V_{Cr}^{\bullet\bullet}$ are consumed (Eq. 5). According to the literature [19, 20], solid-state diffusion is the limiting step during chromia growth. It results of two parallel diffusion fluxes of vacancies: $V_O^{\bullet\bullet}$ from the internal to the external interface, $V_{Cr}^{\bullet\bullet}$ from the external to the internal interface. In the internal subscale, the major point defect is therefore $V_O^{\bullet\bullet}$ leading to a n-type semiconduction. In the external subscale, predominant point defect is $V_{Cr}^{\bullet\bullet}$ giving rise to a p-type semiconduction. If Cr and O vacancies meet, it could lead to vacancy annihilation according to a Schottky equilibrium (Eq. 6). This reaction becomes statistically significant when Cr and O vacancy concentrations are themselves together significant, i.e., at the intermediate interface between subscales and could explain observations on dark-field-STEM images (Fig. 2b). Other large voids (~ 100 nm) are found either in the equiaxis part or in the columnar layer (see Fig. 2) and may be explained by vacancies condensation. Moreover, the outward growth of the external layer added to the compressive stress may explain the columnar morphology that is obtained in the external part. Figure 8 summarizes the model. It should also be mentioned that if point defects are generated in the bulk Cr_2O_3 and measured by

Table 3 Schottky-type red-ox compensation in Cr_2O_3

| Process | Equilibrium | Mass-action term |
|------------|---|--|
| Reduction | $O_2^{\times} \rightleftharpoons 1/2O_2 + V_O^{\bullet\bullet} + 2e'$ | $K_{red} = [V_O][e']^2 \cdot p(O_2)^{1/2}$ |
| Oxidation | $3/2O_2 \rightleftharpoons 2V_{Cr}^{\bullet\bullet} + 3O_O^{\times} + 6h^{\bullet}$ | $K_{ox} = [V_{Cr}^{\bullet\bullet}]^2 [h^{\bullet}]^6 \cdot p(O_2)^{-3/2}$ |
| Ionization | $Nil \rightleftharpoons e' + h^{\bullet}$ | $K_i = [e'] [h^{\bullet}]$ |
| Schottky | $Nil \rightleftharpoons 2V_{Cr}^{\bullet\bullet} + 3V_O^{\bullet\bullet}$ | $K_S = [V_{Cr}^{\bullet\bullet}]^2 [V_O^{\bullet\bullet}]^3 = K_{ox} \cdot K_{red}^3 \cdot K_i^{-6}$ |

Table 4 Equilibria in Cr_2O_3

| Process | Equilibrium | Equilibrium number |
|-------------------------|--|--------------------|
| Sorption | $O_2 + s \rightleftharpoons 2O-s$ | 1 |
| External half-reactions | $O-s + V_O^{\bullet\bullet} + 2e' \rightleftharpoons O_O^{\times} + s$ | 2 |
| | $3O-s \rightleftharpoons 2V_{Cr}^{\bullet\bullet} + 3O_O^{\times} + 6h^{\bullet} + 3s$ | 3 |
| Diffusion | $V_O^{\bullet\bullet}$ | |
| | $V_{Cr}^{\bullet\bullet}$ | |
| Internal half-reactions | $Cr \rightleftharpoons 2Cr_{Cr}^{\times} + 3V_O^{\bullet\bullet} + 6e'$ | 4 |
| | $Cr + 2V_{Cr}^{\bullet\bullet} + 6h^{\bullet} \rightleftharpoons 2Cr_{Cr}^{\times}$ | 5 |
| Schottky | $2V_{Cr}^{\bullet\bullet} + 3V_O^{\bullet\bullet} \rightleftharpoons Nil$ | 6 |

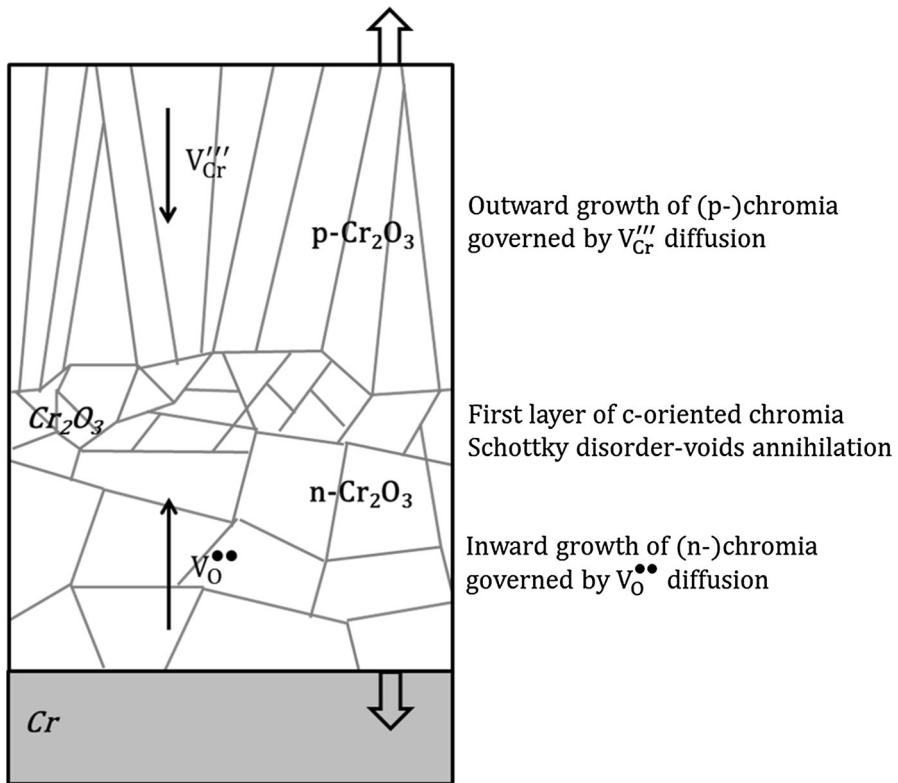


Fig. 8 Proposed mechanism of n- and p-type chromia growth controlled by anionic and cationic vacancies

PEC techniques, they diffuse probably at grain-boundaries (two proposals mutually compatible and consistent).

The presence of a n-chromia below the p-chromia is in the present case governed by oxygen vacancies. This result confirms the study from Ledoux et al. [24] where n-chromia was grown with an anionic mode at a low $p(O)_2$ below a Mn spinel. It may be thought that when the n-chromia is below another oxide layer—in our case, the p-chromia—it leads n-chromia to grow by an anionic mode (inward growing). It can be supposed that single n-chromia can also be grown with a cationic mode (outward growing), thanks to chromium interstitials in agreement with other work [22].

Conclusion

The association of photoelectrochemical and microscopic characterization techniques has permitted to reveal a duplex n- and p-type chromia scale with a peculiar structure. The internal n-chromia has equiaxed grains and presents an inward growing; the p-external part is characterized by columnar grains and presents an

outward growing. The identification of a $\langle 0001 \rangle$ oriented chromia interphase between these two distinct morphologies makes possible to propose a growth mechanism for the duplex chromia. In this model, the diffusion of both oxygen and chromium vacancies is able to take into account experimental results presented in this work.

Acknowledgments This work has benefited from the support of the PSEUDO project of the French National Research Agency (ANR) and was performed within the framework of the Centre of Excellence of Multifunctional Architected Materials “CEMAM” n°AN-10-LABX-44-01 funded by the “Investments for the Future” Program. Special acknowledgments are given to Gilles Renou for his precious help on TEM microscope.

References

1. C. Wagner, *Annual Review of Materials Science* **7**, 1977 (1).
2. J. H. Chen, P. M. Rogers and J. A. Little, *Oxidation of Metals* **47**, (5/6), 1997 (381).
3. P. Kofstad and K. P. Lillerud, *Journal of the Electrochemical Society* **127**, 1980 (2410).
4. F. Lebreau, M. M. Islam, B. Diawara and P. Marcus, *Journal of Physical Chemistry C* **118**, 2014 (18133).
5. Crawford J. A. Crawford and R. W. Vest, *Journal of Applied Physics* **35**, 1964 (2413).
6. A. Holt and P. Kofstad, *Solid State Ionics* **69**, 1994 (127).
7. S. Henry, J. Mougou, Y. Wouters, J.-P. Petit and A. Galerie, *Materials at High Temperatures* **17**, (2), 2000 (231).
8. K. P. Lillerud and P. Kofstad, *Journal of the Electrochemical Society* **127**, 1980 (2397).
9. D. Caplan and G. I. Sproule, *Oxidation of Metals* **9**, (5), 1975 (459).
10. F. Di Quarto, C. Sunseri, S. Piazza and M. C. Romano, *The Journal of Physical Chemistry B* **101**, (14), 1997 (2519).
11. Y. Madi, L. Latu-Romain, S. Mathieu, V. Parry, J.-P. Petit, M. Vilasi and Y. Wouters, *Corrosion Science* **87**, 2014 (218).
12. L. Latu-Romain, Y. Madi, S. Mathieu, F. Robaut, J.-P. Petit and Y. Wouters, *Corrosion Science* **101**, 2015 (193).
13. L. Latu-Romain, S. Mathieu, M. Vilasi, G. Renou, S. Coindeau, A. Galerie, Y. Wouters, *Oxidation of Metals*, **under press** (2016)
14. Y. Wouters, L. Marchetti, A. Galerie and J.-P. Petit, *Corrosion Science* **50**, 2008 (1122).
15. E. F. Rauch and M. Véron, *Materials Characterization* **98**, 2014 (1).
16. J. Mougou, T. Le Bihan and G. Lucazeau, *Journal of Physics and Chemistry of Solids* **62**, 2001 (553).
17. W. W. Gärtner, *Physical Review* **116**, 1959 (84).
18. M. A. Butler, *Journal of Applied Physics* **48**, 1977 (1914).
19. K. P. Lillerud and P. Kofstad, *Journal of the Electrochemical Society* **127**, (11), 1980 (2397).
20. K. Taneichi, T. Narushima, Y. Iguchi and C. Ouchi, *Materials Transactions* **47**, (10), 2006 (2540).
21. P. Sarrazin, A. Galerie, J. Fouletier in “*Mechanisms of High Temperature Corrosion*”, Trans Tech Publications, Ltd, (2008)
22. K. P. Lillerud and P. Kofstad, *Oxidation of Metals* **17**, (1/2), 1982 (127).
23. K. J. W. Atkinson, R. W. Grimes, M. R. Levy, Z. L. Coull and T. English, *Journal of the European Ceramic Society* **23**, 2003 (3059).
24. X. Ledoux, S. Mathieu, M. Vilasi, Y. Wouters, P. Del-Gallo and M. Wagner, *Oxidation of Metals* **80**, 2013 (25).